Draft version January 28, 2022
Preprint typeset using LaTeX style emulateapj v. 5/2/11

STELLAR MASSES AND STAR FORMATION RATES FOR 1M GALAXIES FROM SDSS+WISE

Yu-Yen Chang[1], Arjen van der Wel[1], Elisabete da Cunha[1,2], Hans-Walter Rix[1]

Draft version January 28, 2022

ABSTRACT

We combine SDSS and WISE photometry for the full SDSS spectroscopic galaxy sample, creating SEDs that cover λ=0.4-22μm for an unprecedented large and comprehensive sample of 858,365 present-epoch galaxies. Using MAGPHYS we then model simultaneously and consistently both the attenuated stellar SED and the dust emission at 12μm and 22μm, producing robust new calibrations for monochromatic mid-IR star formation rate proxies. These modeling results provide the first mid-IR-based view of the bi-modality in star formation activity among galaxies, exhibiting the sequence of star-forming galaxies ("main sequence") with a slope of $d\log SFR/d\log M_* = 0.80$ and a scatter of 0.39 dex. We find that these new star-formation rates along the SF main sequence are systematically lower by a factor of 1.4 than those derived from optical spectroscopy. We show that for most present-day galaxies the 0.4-22μm SED fits can exquisitely predict the fluxes measured by Herschel at much longer wavelengths. Our analysis also illustrates that the majorities of stars in the present-day universe is formed in luminous galaxies ($\sim L^*$) in and around the 'green valley' of the color-luminosity plane. We make the matched photometry catalog and SED modeling results publicly available.

Subject headings: catalogs — galaxies: statistics — galaxies: stellar content — galaxies: star formation — infrared: galaxies —

1. INTRODUCTION

Some of the most basic and important constraints on galaxy formation models are the present-day stellar mass function and the distribution of star formation among galaxies with different masses. The Sloan Digitital Sky Survey (SDSS, Blanton et al. 2005; Adelman-McCarthy et al. 2008; Padmanabhan et al. 2008) has provided the measurements that underlie our current knowledge of the stellar masses (M_*) and star formation rates (SFRs) of large samples of galaxies (e.g., Brinchmann et al. 2004). The SDSS multi-wavelength (*ugriz*) imaging has been used to estimate luminosities and mass-to-light ratios (e.g., Baldry et al. 2012). The resulting stellar masses have been demonstrated to correlate tightly with total, dynamical mass estimates (Taylor et al. 2011) with a scatter of only 0.13 dex. Brinchmann et al. (2004) use the Charlot & Longhetti (2001) photoionization model to convert nebular emission line fluxes from SDSS spectroscopy into SFRs. Salim et al. (2007) provided SFRs based on GALEX UV fluxes. But these previous SDSS studies did not account for the extra information enclosed in dust emission, when estimating both star formation rate and dust attenuation. Here we present alternative M_* and SFR estimates by extending the photometric wavelength coverage of the SDSS spectroscopic sample to the near- and mid-infrared as enabled by WISE (Wright et al. 2010), which provides allsky coverage at $3-22\mu$m.

The 3.4μm and 4.5μm bands sample the Rayleigh-Jeans tail of the stellar spectral energy distribution (SED), which avoids the contribution from hot, young stars which can dominate at shorter wavelenghts. In addition, extinction is usually negligible in these bands. As a result, near-infrared luminosities provides fairly accurate and precise stellar mass estimates, even in the absence of any other photometric or spectroscopic information (Meidt et al. 2014). Many authors have used $3-5\mu m$-photometry from Spitzer or WISE to compare with stellar mass estimates derived from photometry at $2\mu m$ and below (e.g., Li et al. 2007; Zhu et al. 2010; Jarrett et al. 2013). Here we combine SDSS and WISE data to generalize the use $3-5\mu$m photometric information in estimating stellar masses.

Mid-infrared emission traces star-formation activity through the well-known correlation with PAH emission, sampled by the WISE 12μm band, and through the correlation with thermal radiation from dust, sampled by the WISE 22μm band. A number of authors have compared star-formation rates from Brinchmann et al. (2004), based on optical emission lines, with mid-IR luminosities from WISE (e.g., Donoso et al. 2012; Lee et al. 2013; Wen et al. 2013, 2014); these studies do not model the mid-IR luminosity to obtain SFRs that are independent of the emission-line based SFRs.

Here we take the important step to include the full WISE photometry and employ SED modeling that consistently treats the stellar emission along with the dust extinction *and* emission. This will result in more robust masses and star-formation rates for dusty galaxies and, in general, an alternative to the emission-line based SFRs from Brinchmann et al. (2004) for the full SDSS spectroscopic galaxy sample. This is not been attempted before for large samples of galaxies. Jarrett et al. (2013) provided a detailed multi-wavelength study of a small number of objects and will provide an important benchmark to test our results. Brown et al. (2014) performed SED fits across the UV to mid-IR wavelength in an exercise similar in approach as what we present here, but for those authors the focus lay on producing a set of representative templates: stellar mass and SFR estimates are not presented or discussed. Cluver et al. (2014) analyze

[1] Max-Planck Institut für Astronomie, Königstuhl 17, D-69117, Heidelberg, Germany; e-mail: yu-yen.chang@cea.fr
[2] Centre for Astrophysics and Supercomputing, Swinburne University of Technology, Hawthorn, Victoria 3122, Australia

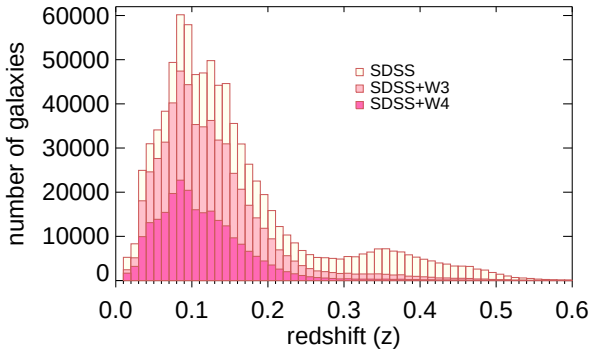

FIG. 1.— Redshift distribution of the SDSS galaxy sample. 98.24% of the objects are detected in at least one WISE band. The subsamples with $> 2\sigma$ detections in W3 (12μm) and W4 (22μm) are highlighted.

the mid-IR properties of the large GAMA sample, but there Hα-based SFRs were used as a calibrator for the mid-IR luminosities from WISE. As such, our study is the first to use the mid-IR luminosities of a large sample of galaxies (the full SDSS spectroscopic galaxy sample) to estimate their SFRs in a manner that is entirely independent of optical emission line luminosities and other external calibrators.

This paper is organized as follows. In Section 2 we will describe the SDSS and WISE photometric datasets, with a particular focus on total flux measurements for extended sources. In Section 3 we will describe MAGPHYS (da Cunha et al. 2008), the SED fitting code, and test the robustness of the fitting results. In particular, we will test how well MAGPHYS can predict, with the available wavelength coverage of $0.4-22\mu$m, the total IR luminosity. Furthermore, we will compare our M_* and SFR estimates with the Brinchmann et al. (2004) measurements. In Section 4 we will describe the publicly released catalog with the fitting results for the entire SDSS spectroscopic sample (~800,000 galaxies). In Section 5 we will show, as an illustration, how star formation is distributed over galaxies with different masses and colors.

We use AB magnitudes and adopt the cosmological parameters (Ω_M,Ω_Λ,h)=(0.30,0.70,0.70) and adopt the Chabrier (2003) stellar initial mass function.

2. DATA

We use the SDSS spectroscopic galaxy sample as compiled in the New York University Value-Added Galaxy Catalog (NYU-VAGC, Blanton et al. 2005; Adelman-McCarthy et al. 2008; Padmanabhan et al. 2008) [3], which contains 858,365 galaxies with reliable redshift measurements (`OBJTYPE`=GALAXY, `Zwarning`=0), distributed as shown in Figure 1. We adopt `MODELFLUX` and `MODELFLUX_IVAR` as the flux measurements and their uncertainties, with galactic extinction corrections as prescribed by Schlafly & Finkbeiner (2011). To account for the uncertainty in the extinction law, we propagate an uncertainty in $R_V = 3.1 \pm 0.2$ in our flux uncertainty estimates. Minimum uncertainties are added in quadrature: 0.05 mag for the u band and 0.02 mag for the $griz$ bands. This is aimed at preventing from small systematic uncertainties to dominate the our goodness-of-fit assessment and the uncertainties in our derived parameters. In case of catastrophic failures in the photometric measurements, which occasionally occurs in the u and z bands, we omit these data points from the fits.

The SDSS parent sample is cross-matched with the AllWISE source catalog[4]. The vast majority of galaxies have counterparts (98.24%), identified as the brightest object within a search radius of 6 arcsec, similar to the WISE PSF. In line with the approach taken by Donoso et al. (2012) and Yan et al. (2013), most matches (99.08%) are found within a radius of 3 arcsec and the majority (91.20%) do not have multiple matches within 6 arcsec. We provide a flag ($FLAG\_W$) that indicates if there are one or more matches, but we do not exclude any matched sources *a priori*. Various flux measurements are provided by the AllWISE catalog. In order to minimize the effects of source blending we use the `W?mpro` and `W?sigmpro` flux measurements and their uncertainties. These are profile-fitted photometry measurements, performed simultaneously on neighboring sources, using the point spread function (PSF) as the source model. Most of the galaxies with counterparts have significant W1 and W2 flux measurements (98.83%). For W3 and W4, many of the flux measurements amount to upper limits (29.10% and 70.89%, respectively). The redshift distributions of galaxies with $> 2\sigma$ W3 and W4 detections are shown in Figure 1. We will provide flags to indicate which galaxies have detections, and which have upper limits. The usefulness of the upper limits will depend on the goals of the user.

Galaxies are typically smaller than the WISE PSF, but the amount by which `W?mpro` underestimate the total flux due to the spatial extent of the sources is not necessarily negligible. The W1, W2, and W3 bands all have very similar PSFs with FWHM$\sim 6-7$ arcsec, while the W4 PSF is larger (~ 12) arcsec. We investigate the missing light fraction for W1, W2, and W3 by generating with `galfit` (Peng et al. 2010) a series of simulated light distributions with 2-dimensional Sérsic profiles convolved with the W1 PSF models provided by Aniano et al. (2011), and inserted into empty sections of real W1 images[5]. Then, we use `galfit` to fit the PSF model to the simulated images to measure the PSF profile flux. We find that the difference between the PSF profile flux and the true, total flux is mostly a function of the effective radius of the Sérsic profile, and hardly depends on input flux, axis ratio, or Sérsic index. For a typical size of 5 arcsec, we find that Δm varies from 15.63 mag for Sérsic index $n = 1$ to 15.65 mag for Sersic index $n = 4$. Based on these simulations we find that the PSF profile magnitude underestimates the total flux by

$$\Delta m = 0.10 + 0.46\log(R_e) + 0.47\log(R_e)^2 + 0.08\log(R_e)^3, \quad (1)$$

where R_e is the effective radius in arcsec. This correction is used whenever the size is larger than $R_e = 0.5$ arcsec. We propagate the uncertainty in the adopted radius into Delta m, which is in turn propagated into the flux uncertainty in flux.

We use the r-band effective radii and apply a system-

[3] http://sdss.physics.nyu.edu/vagc/

[4] http://wise2.ipac.caltech.edu/docs/release/allwise/

[5] http://www.astro.princeton.edu/~ganiano/Kernels/Ker_2012_May/PSF_f

atic correction of a factor 1.5 ± 0.2 downward to to convert from optical size to near-IR size. This conversion is based on the analysis of (Vulcani et al. 2014), who consistently measured sizes for a large set of galaxies across the wavelength range 0.4 to 2.2 μm. These corrected sizes and Equation 1 are then used to correct the W1, W2, and W3 fluxes. We use r-band effective radii are measured by Simard et al. (2011) when available, and otherwise `deVRad` or `expRad from` the SDSS catalog as appropriate. We prefer the Simard et al. (2011) measurements as their fitting methodology (two-dimensional light profiles) is more similar to the methodology used by Vulcani et al. (2014) (the SDSS pipeline fits one-dimensional light profiles). We note that the difference between the two versions of our W1/2/3 magnitude corrections is small: for objects for which both measurements are available the median difference is 0.03 mag, and the random scatter 0.14 mag. These uncertainties are small compared to the uncertainties in stellar masses and SFRs derived below. These final flux measurements, along with the applied corrections, are listed in the public catalog (see Section 4). The median correction is 0.25 mag, with a scatter of -0.07 (16%-ile) and +0.18 (84%-ile). Corrections for W4, for which the PSF is twice as wide, are not made.

To account for possible systematic uncertainties of the WISE and SDSS photometric systems and further systematic differences between the total flux measurements we adopt and propagate 0.1 mag uncertainties for all WISE fluxes.

3. SED MODELING

3.1. *Method*

We use MAGPHYS to fit the photometric SED (da Cunha et al. 2008, 2012) [6]. The public version of MAGPHYS contains 50,000 stellar population template spectra (the optical photometric library) and 50,000 PAH+dust emission template spectra (the infrared photometric library). The stellar emission templates use the Bruzual & Charlot (2003) stellar population synthesis models and are generated for a wide range of star formation histories parameterized as exponentially-declining models with superimposed random bursts of star formation.

The SEDs are computed by adding the individual spectra of all simple stellar populations, weighed by mass. The original MAGPHYS library was constructed for modeling IR-luminous, star-bursting galaxies. The original MAGPHYS library from the public version with 50,000 stellar population template spectra was constructed for modelling star-forming galaxies and we extended the optical library to include 25,000 additional templates for more passive stellar populations.

The infrared templates describe emission by dust. The total dust luminosity over 3 to 1000μm has components of emission from PAHs and dust with a range of temperatures. The model contains the ambient (diffuse) interstellar medium and star-forming regions (birth clouds). Because stars are born in dense molecular clouds which dissipate typically after 10^7 years, the SED of young stellar populations are attenuated by both dust in the birth clouds and dust in the ambient ISM, while the SED of older populations is only attenuated by dust in the diffuse ISM. The absorbed light is assumed to be re-emitted in the mid- and far-infrared, requiring conservation of energy.

MAGPHYS fits SEDs in the observed frame. Therefore, we generate libraries with model fluxes in the observed frame for a series of narrow redshift bins ($\delta z = 0.0001$) that span the range of our sample. The fitting process for each individual galaxy is then expediated in two ways. First, we only consider optical templates with similar $(g-i)_{\rm model}$ colors as the observed $(g-i)_{\rm data}$ color. To be precise, we select templates with $|(g-i)_{model} - (g-i)_{data}| < 0.05 + \sigma[(g-i)_{data}]$, where σ refers to the uncertainty. This method works for any two filters, and here we choose $g-i$. The selection is inclusive enough to avoid changes in the results: none of the models eliminated from consideration have significant likelihood values. We check that we would get similar results if we fitted the whole model library. Second, we draw a random set of 1,000 infrared templates from the total set of 50,000 templates. Since our data do not sample the thermal peak, we cannot stringently constrain the dust temperature distribution, rendering full exploration of parameter space useless. As a test we compare the results based on the full and reduced infrared libraries and find no systematic differences (smaller than 0.01 dex for both stellar mass and SFR) in the fitting results and no increases or decreases in the formal fitting uncertainties.

In a small number of cases we find that MAGPHYS allows the presence of an unrealistically large amount of cold dust. In order to avoid this, we put a mild constraint on the model 250μm luminosity based on the maximum observed 250μm-to-22μm flux ratios (Chary & Elbaz 2001): $L\nu_{250\mu\rm m}[L_\odot/Hz] < 85.7 \times (L\nu_{22\mu\rm m} + \sigma(L\nu_{22\mu\rm m}))\ [L_\odot/Hz]$, which is $\sim$6 times the typical ratio. We will investigate the precision of our predicted total IR luminosities below, in § 3.3.

Given our 10 flux constraints (SDSS$ugriz$; W1−4; $L\nu_{250\mu\rm m}$ limit) χ^2 is calculated for each model in the library. For each model parameter the posterior probability distribution can be generated by taking the prior probability distribution (from the full library) and assign weights $exp(-\chi^2/2)$ to each of the models. In doing so we marginalize over all other model parameters and assume that the likelihood of a given model given the data is proportional to $exp(-\chi^2/2)$. We adopt the 50 percentile value – that is, the median – as the best estimate. In practice, in the case of upper limits, we assumed zero flux with the upper limit as the error bar.

Rest-frame fluxes are calculated using the observed fluxes and colors. Analogous to Holden et al. (2012) we derive for each redshift z bin a linear fit between, on the one hand, observed-frame magnitudes (m_{obs1}, m_{obs2}) of the templates in the filters straddling the desired rest-frame band, and, on the other hand, the rest-frame magnitude (m_0) of the same templates: $m_0 = m_{obs1} + A(z) \times (m_{obs1} - m_{obs2}) + B(z)$. Then, for each galaxy in the sample, we use the observed magnitudes and the values of $A(z)$ and $B(z)$ to compute its rest-frame magnitudes. We also adopt this technique to calculate rest-frame 12μm and 22μm luminosities. The basic result of the SED MAGPHYS modelling for each object, is a joint

[6] http://www.iap.fr/magphys

PDF for the 16 parameters, which we then characterize by the median and the percentiles of the marginalized distributions.

FIG. 2.— Rest-frame $u-r$ vs. $r-z$ distribution for our SDSS+WISE sample, color-coded according to the fraction of objects that lie on the star-forming sequence or significantly below according to their full SED fit (see Section 4). The clearly distinct color-color distributions of star-forming and quiescent galaxies validate the assumption that a color-color diagram can be effectively used to distinguish the two types of galaxies, as is often done at high redshift. The labels correspond to the objects for which the SEDs are shown in Figures 3, 4, 5, and 6.

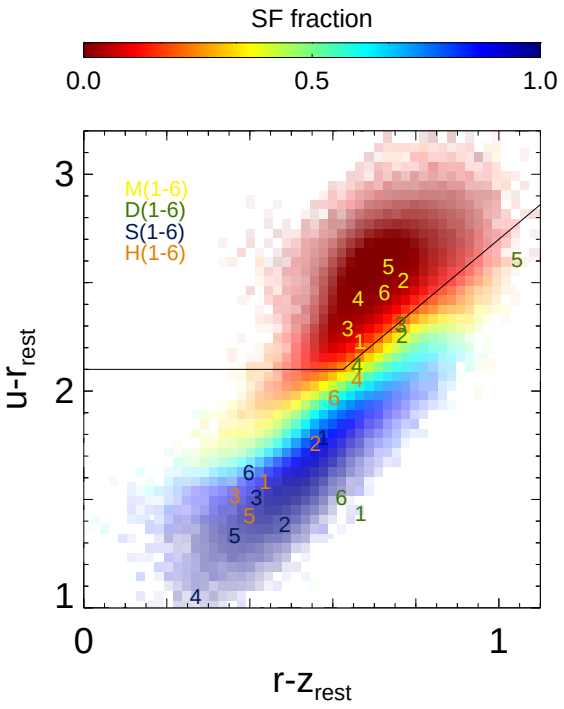

3.2. *Sample SEDs*

The galaxies in our sample span a large range in stellar mass, star formation rates and colors (Figure 2). In Figures 3, 4, and 5 we show examples of SEDs and fitting results across the entire parameter space populated by our sample. Figure 3 shows six massive galaxies ($M_* \sim 10^{11}\ M_\odot$ with little or no ongoing star formation ($\lesssim 1\ M_\odot\ \mathrm{yr}^{-1}$). The characteristic red optical SEDs are accompanied by non-neglible mid-IR emission arising from a combination of dust heated by evolved stars and traces of star formation. Figure 4 shows reddened galaxies with significant star formation activity, where the IR luminosity often exceeds the optical/NIR luminosity. Figure 5 shows blue star-forming galaxies, with little or no extinction.

To demonstrate the quality of the fits we show in Figure 7 the chi-square distribution across parameter space (M_*, SFR, colors). χ^2 is the the goodness-of fit parameter for the best-fitting model, but not, formally speaking, the reduced chi-squared of the best-fitting model as discussed by Smith et al. (2012). The generally low values of χ^2 imply that our library of models is sufficiently extensive.

3.3. *Verification of total IR Luminosities with Herschel*

MAGPHYS balances the energy absorbed in the UV/optical and the energy released in the IR, such that the inferred total IR luminosity can be expected to be correct if the optical/NIR SED is accurate. Still, since the WISE 12μm and 22μm bands do not sample the thermal peak of the dust emission, it is important to test the robustness of the fitting results, in particular the star-formation rates and dust luminosities.

Herschel-ATLAS provides PACS and SPIRE photometry over the wavelength range 100-500μm. These observations sample the total dust emission more directly than WISE. For the subsample of 285 galaxies that fall within the 16 square degree footprint of the publicly available part of Herschel-ATLAS (Eales et al. 2010; Ibar et al. 2010; Pascale et al. 2011; Rigby et al. 2011; Smith et al. 2011) we verify the precision and accuracy of our inferred total IR luminosity.

Our SDSS+WISE-based models succesfully predict of total IR luminosities and star-formation rates from SDSS+WISE+Herschel photometry, as illustrated in Figure 6). Even though the marginalized probability distributions for the dust luminosity and star-formation rate are tightened when Herschel photometry is added, we find no systematic offset (0.00 dex) between the star-formation rates. Furthermore, the scatter (0.19 dex) is consistent with the formal confidence intervals (see Figure 8). The uncertainties of $SFR \sim 10^{-4} M_\odot/yr$ galaxies are large and dust luminosities are poorly constrained.

3.4. *The Public Catalog*

We provide two public catalogs[7]. They both contain all 858,365 galaxies from the SDSS spectroscopic galaxy sample with good redshift measurements as described in Section 2. Table 1 contains the input data (ID, redshift, fluxes, Galactic extinction). Table 2 contains the modeling results from MAGPHYS, V_{max} (see below), rest-frame luminosities, and a set of flags. We recommend to use the MAGPHYS modeling results for objects with FLAG=1 (633,205 out of 858,365). These are all $z < 0.2$ galaxies with reliable aperture corrections based on size measurements from Simard et al. (2011) ($FLAG\_R = 1$), good WISE photometry ($FLAG\_W? = 1$ or 2), and good-quality SED fits ($FLAG\_CHI2 = 1$). This primary sample contains 91.40% of all SDSS galaxies at $z < 0.2$.

Our V_{max} calculation only includes the maximum redshift at which galaxies would be retained in the sample. No low-redshift limit, related to the SDSS bright-magnitude limit, is taken into account. For our purposes of illustrating the distribution of SFR and stellar mass this does not matter given the large volume, but for individual, low-redshift, high-luminosity galaxies the user should keep in mind that our V_{max} cannot be directly used.

4. DISCUSSION

4.1. *Comparison with Brinchmann et al. (2004)*

Stellar masses and SFRs from the MPA-JHU catalogs (Brinchmann et al. 2004) are widely used. The differences between their and our stellar mass estimates are

[7] http://irfu.cea.fr/pisp/yu-yen.chang/sw.html

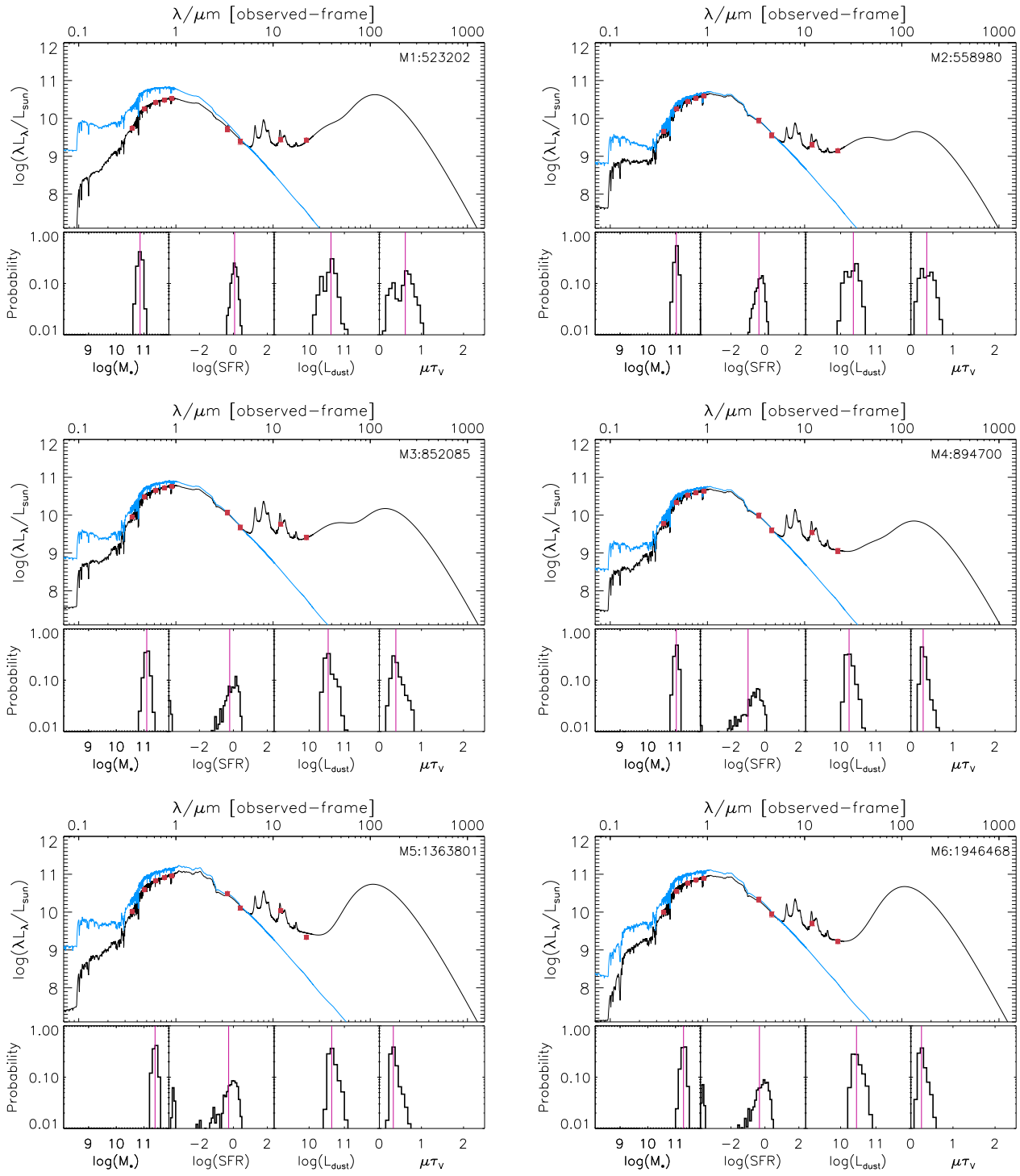

FIG. 3.— Example SEDs and fitting results of six massive, quiescent galaxies. The large sub-panels show the observed fluxes (red points), the best-fitting SEDs (black lines) and the corresponding unattenuated stellar SEDs (blue lines). The smaller panels show the marginalized posterior probability distributions of four models parameters: M_*, SFR, dust luminosity (in solar units), and dust attenuation. The red lines show the median values, which we adopt as best-fitting values of the PDF. The short-hand IDs (M1-6) correspond to the labels in Figure 2.

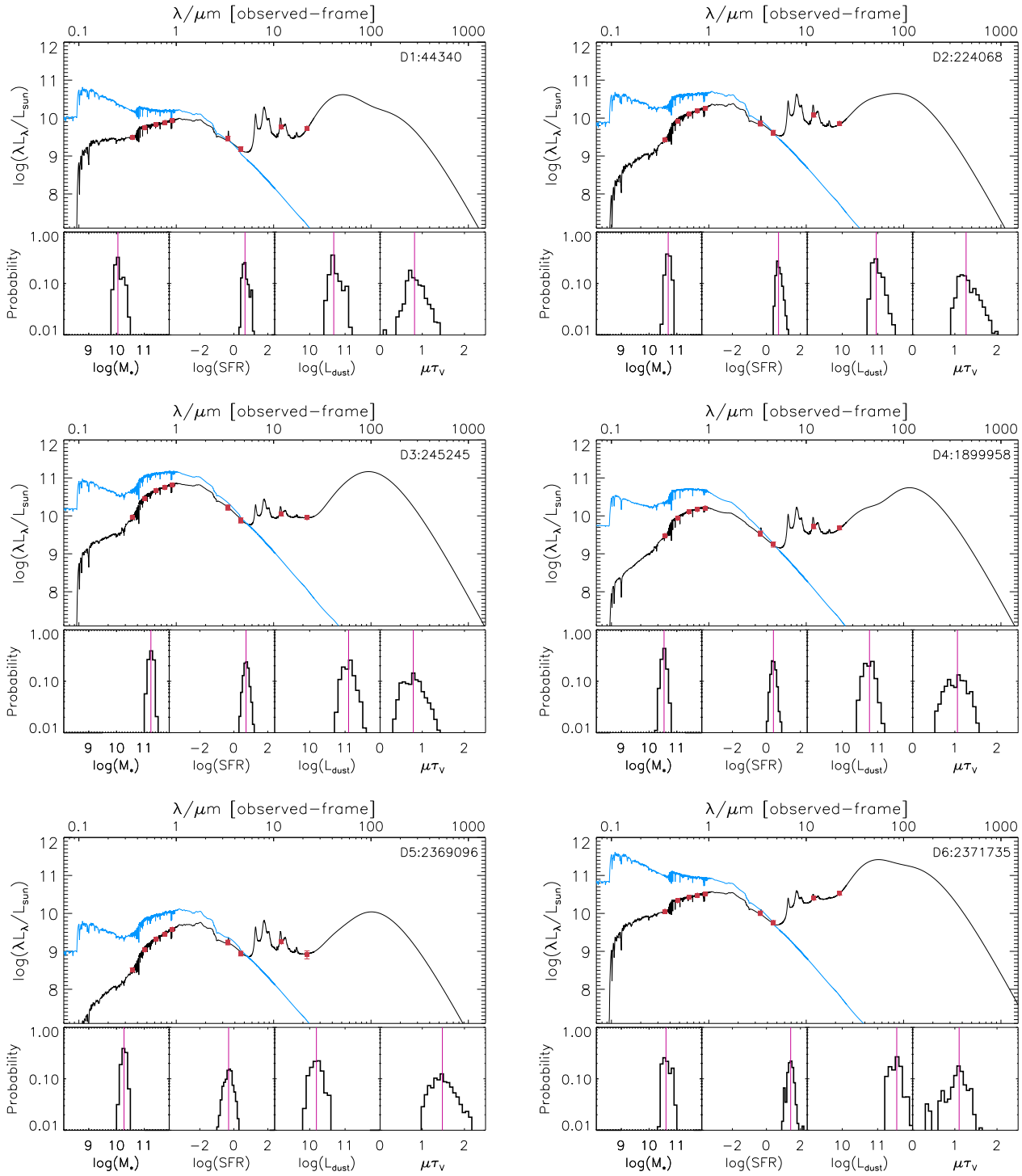

FIG. 4.— Example SEDs and fitting results of six star-forming galaxies , where the optical light is significantly dust-extincted. See Figure 3 for an explanation of the panels, lines, and symbols. The short-hand IDs (D1-6) correspond to the labels in Figure 2.

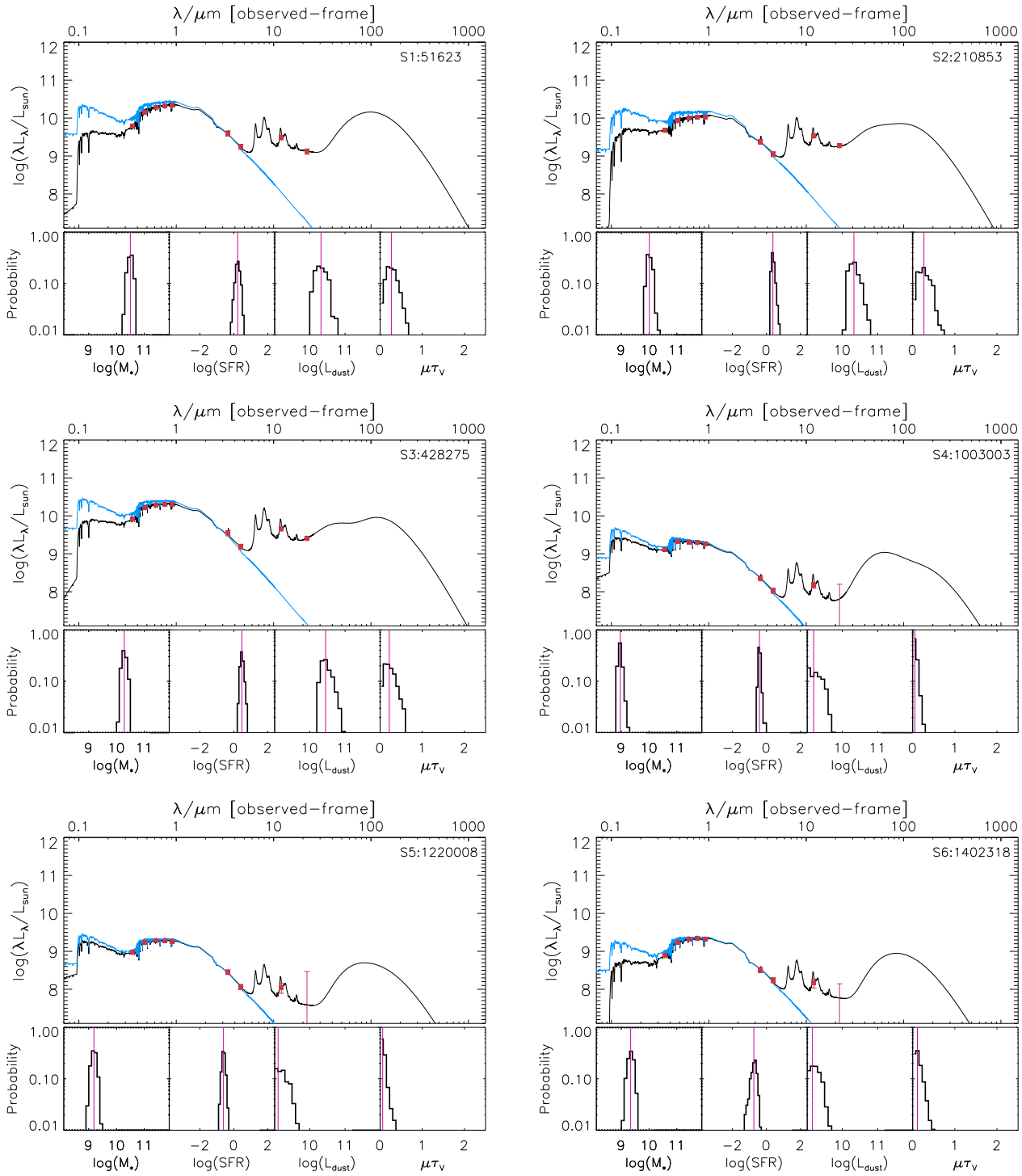

FIG. 5.— Example SEDs and fitting results of six blue, star-forming galaxies , with only modest dust extinction in the optical. See Figure 3 for an explanation of the panels, lines, and symbols. The short-hand IDs (S1-6) correspond to the labels in Figure 2.

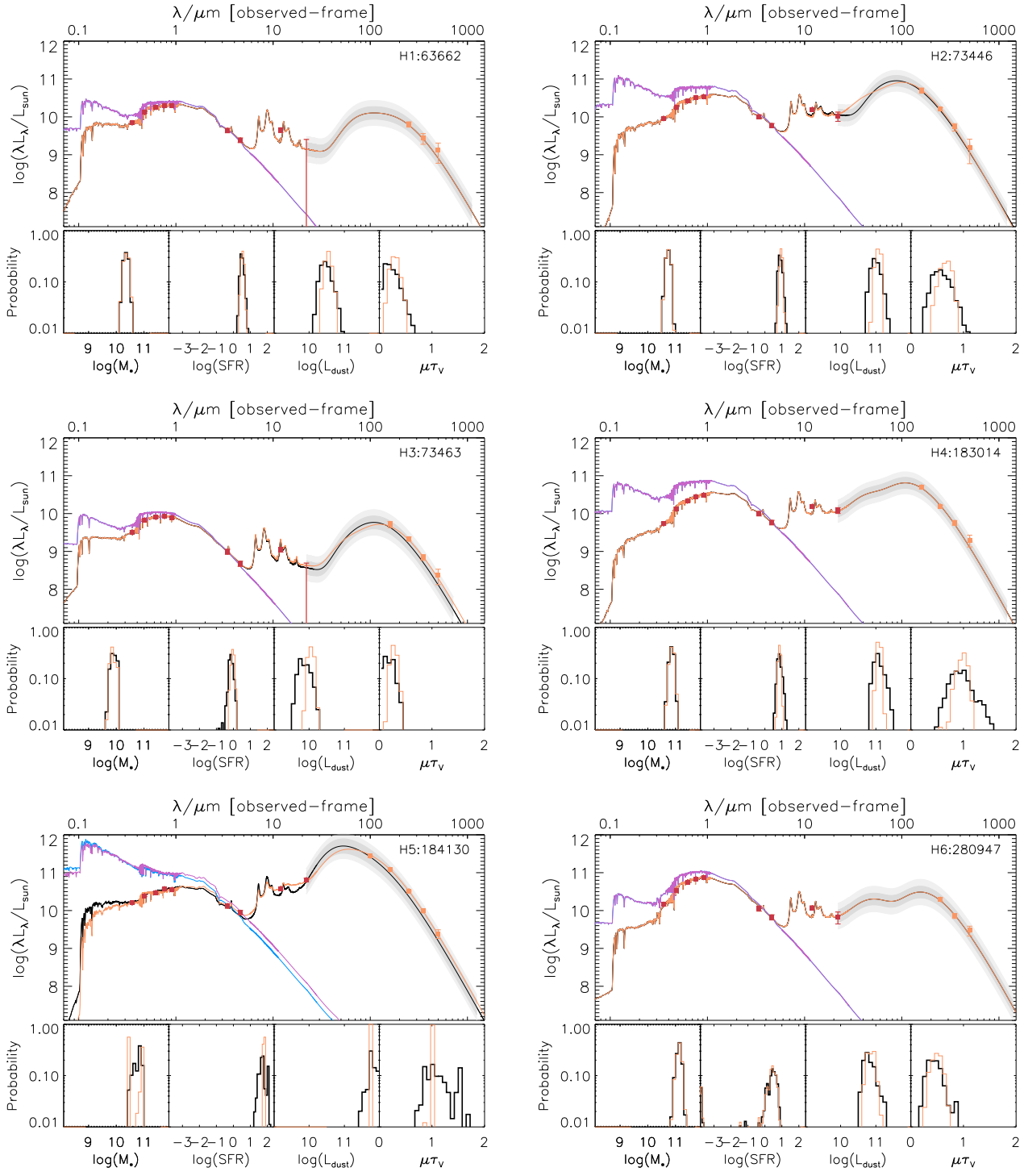

FIG. 6.— Example SEDs and fitting results of six galaxies with Herschel-ATLAS photometry available (orange points) in addition to the SDSS & WISE (red points). The blue and black lines represent fitting results to the SDSS + WISE data only (as in Figure 3), and the dark (light) gray areas represent the 68% (95%) confidence intervals for the far-IR dust SED *predicted* from these fits. The magenta and orange lines represent the best-fitting unattenuated and attenuated SEDs, respectively, when the Herschel-ATLAS SEDs are also simultaneously fitted. The smaller panels show the marginalized posterior probability distributions of four of the model parameters. In all cases, the SDSS+WISE fitting results predict the Herschel photometry well and all results inferred without Herschel data are consistent with the results inferred with Herschel data. However, the constraints on the dust luminosity and dust attenuation parameter are tightened once Herschel photometry is included. The short-hand IDs (H1-6) correspond to the labels in Figure 2.

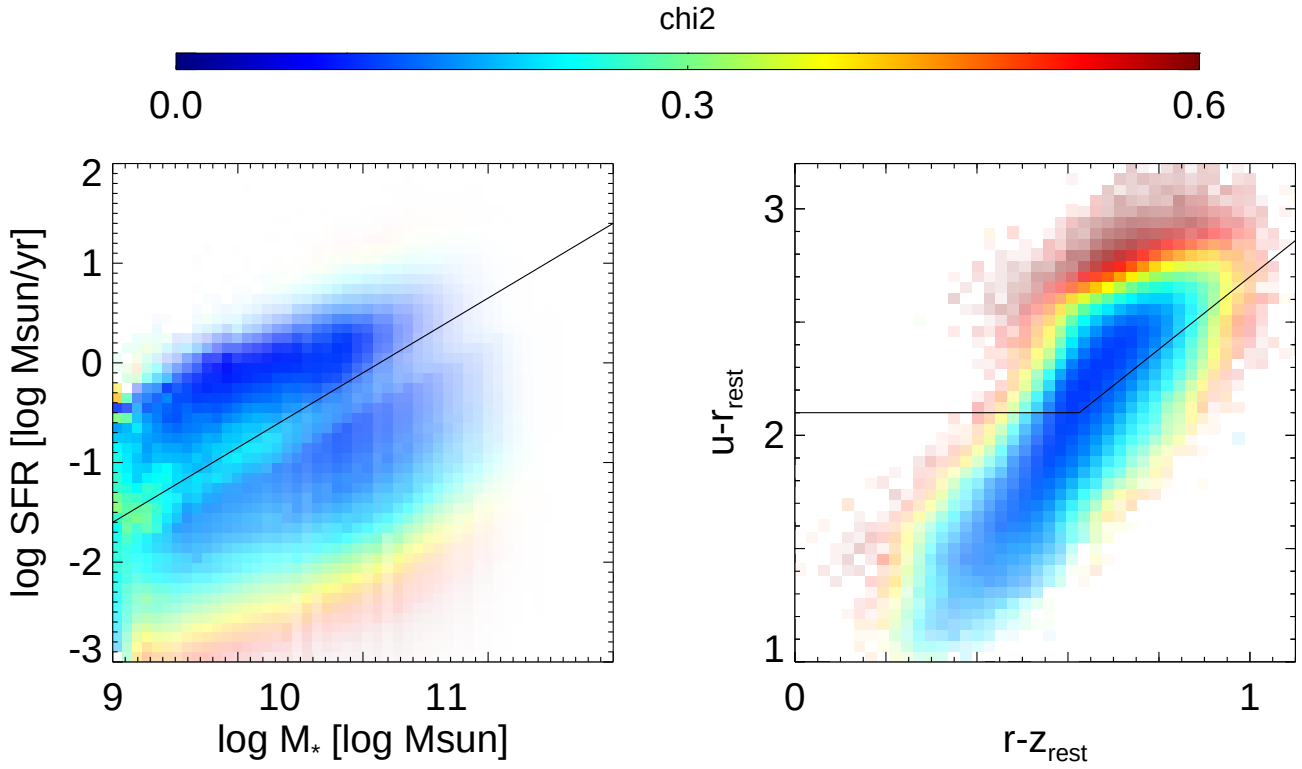

FIG. 7.— Quality of the SED fit, shown in dependence of SFR versus stellar mass (left; also see Figure 9 and Figure 11) and rest-frame $u-r$ vs. $r-z$ (right; also see Figure 2). The color coding is the median chi-square value. Boxcar smoothing in two dimensions considering the uncertainties of the parameters is applied to the color coding and opacity. For star-forming galaxies, the distribution is about uniform.

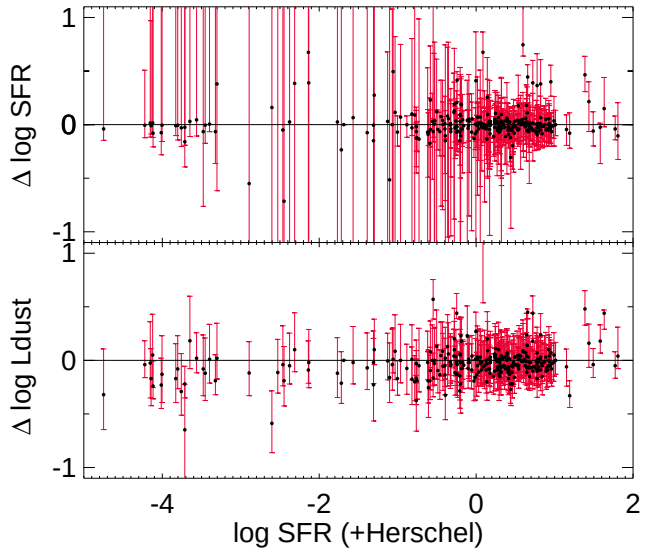

FIG. 8.— *Top:* SFR from the SED fits with only optical (SDSS) and near/mid-IR (WISE) data minus SFR from fits that also include far-IR Herschel data vs. SFR from fits with Herschel data. The objects included here are those that overlap between our SDSS-selected sample and Herschel-ATLAS. Red error bars indicate 68% confidence intervals. *Bottom:* Same as above, but for dust luminosity. Our SDSS+WISE based fitting results are generally consistent with the SDSS+WISE+Herschel-based fitting results.

the addition of WISE 3.4μm and 4.5μm photometry as tracers of stellar mass, and the updated Galactic extinction correction from Schlafly & Finkbeiner (2011). Furthermore, the simultaneous fitting of mid-IR photometry provides a fundamentally different constraint on the dust properties of galaxies than optical photometry and emission line ratios. In addition, dust attenuation laws are also different. In Brinchmann et al. (2004) the adopted slope for the attenuation curve is -0.7, following Charlot & Fall (2000). MAGPHYS has the same slope for diffuse dust, but a steeper slope (-1.3) for birth clouds. Despite these differences, offsets between the two sets of mass estimates are small and insignificant (left-hand panel, Figure 9). The reasons for this are that the same stellar population models and star-formation histories are used and that the impact of the WISE photometry is limited due to the relatively large uncertainties on the total flux measurements.

Larger differences are seen for the SFR estimates. As opposed to the stellar mass estimates, the SFR estimates rely on wholly different tracers in the two cases. Selecting star-forming galaxies by their location in the color-color diagram (Figure 2), we find a median offset across the sample of 0.22 dex and a scatter of $\sim$ 0.3 dex. This offset does not depend on mass or redshift, or even on whether the galaxies have significant 12μm and 22μm detections, but strongly varies with SFR (Figure 9): for high-SFR galaxies our values are large compared to Brinchmann et al. (2004), for low-SFR galaxies our values are small. The anti-correlation between the changes in M_* and SFR is the result of the underlying anti-correlation between

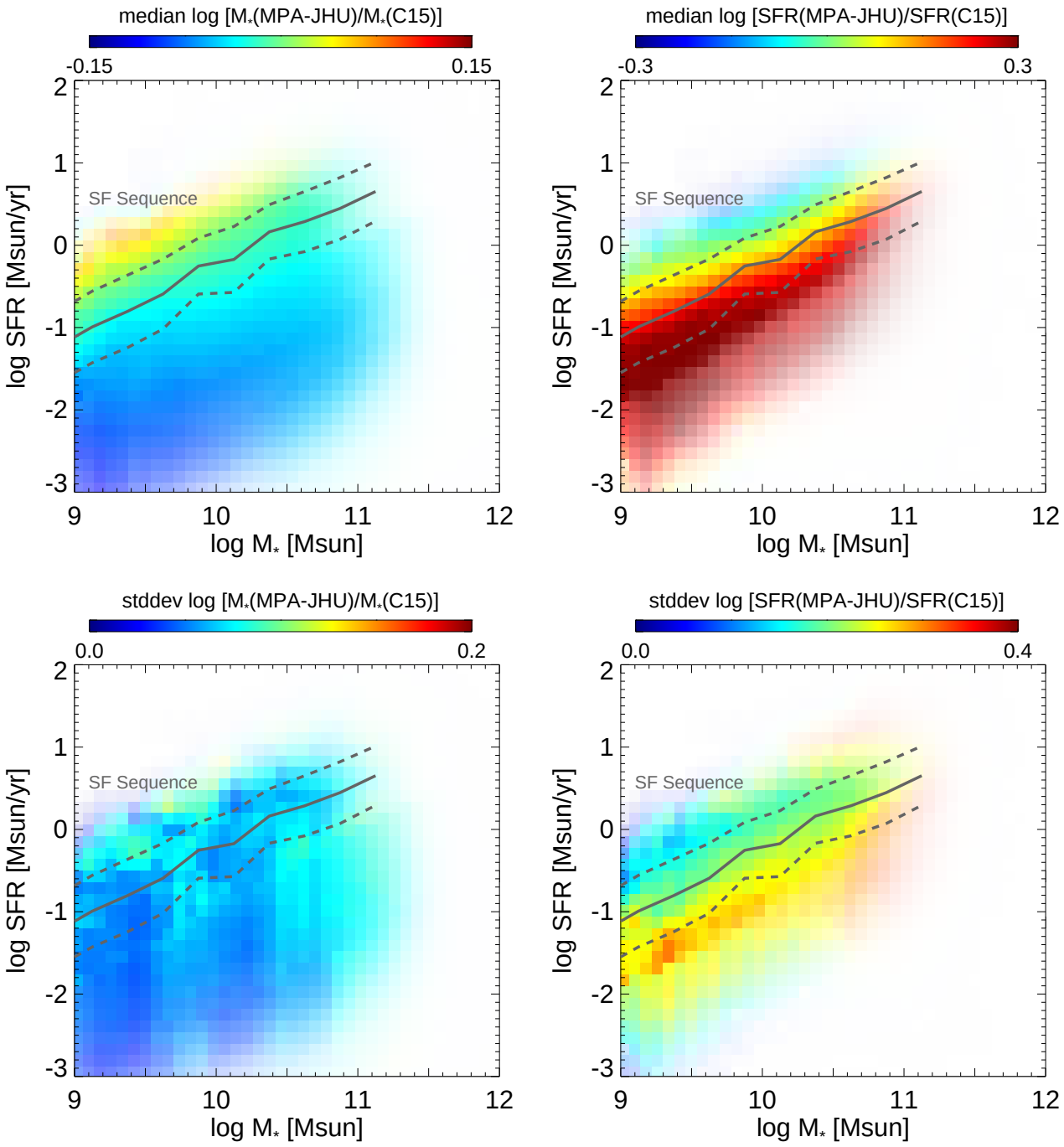

FIG. 9.— Comparison between the MPA-JHU values for M_* and SFR and the values derived here (C15). *Top left:* median difference between the stellar mass estimates. These are always small ($\lesssim$ 0.10 dex). *Bottom left:* scatter in the stellar mass estimates; generally $\lesssim$ 0.15 dex. *Top right:* median difference in SFR. Here we only show star-forming galaxies selected the color-color classification given in the right-hand panel of Figure 2. Across the sample the offset is 0.22 dex. It is strongly SFR-dependent, and ranges from -0.3 dex to +0.3 dex. *Bottom right:* scatter in the SFR estimates, typically 0.3 dex or a factor of two. The grey lines shows the star-forming sequence in Figure 11.

mass to light ratio and sSFR.

4.2. *12μm and 22μm luminosities as SFR indicators*

Another consequence is that our 12μm and 22μm SFR conversions are lower by, respectively, 0.22 dex and 0.10 dex compared to the conversion based on a comparison with the Brinchmann et al. (2004) estimates, as carried out by Lee et al. (2013).

In Figure 10 we show the correlations between 12μm and 22μm luminosities and our SFR estimates. The large downward scatter is due to mid-IR radiation that is not associated with star formation. In particular, the mid-IR luminosities of quiescent galaxies do not reflect star formation activity, but rather circumstellar dust and PAHs heated by evolved stars (e.g., Bressan et al. 2006). Even for many galaxies that are star-forming according to our definition – separated in color-color space (Figure 2; SF galaxies: $(u-r)_{rest} < 2.1$ or $(u-r)_{rest} < 1.6 \times (r-z)_{rest} + 1.1$) – a large fraction of the mid-IR luminosity is not attributed to star formation. Keeping this in mind, we derive the following conversions from mid-IR luminosity to SFR:

$$\log SFR/(M_\odot\ yr^{-1}) = \log L_{12}/L_\odot - 9.18 \qquad (2)$$

and

$$\log SFR/(M_\odot\ yr^{-1}) = \log L_{22}/L_\odot - 9.08, \qquad (3)$$

These relationships are determined by calculating the median values of the SFR in bins of 0.25 dex wide bins in luminosity and performing a linear fit to these median values, weighing by the inverse of the square root of the numer of objects in the bins. The upward scatter (84%-ile minus median) in SFR is 0.20 dex, while the downward scatter (median minus 16%-ile) is 0.60 dex, reflecting non-SF contributions. The scatter obviously depends on luminosity: above $10^{10}\ L_\odot$ the downward scatter is also 0.30 dex.

The 12μm and 22μm values are 0.13 and 0.04 dex higher than the conversions provided by Jarrett et al. (2013), who based their SFRs on GALEX UV fluxes and the standard Spitzer/MIPS 24μm calibration from Rieke et al. (2009). The relatively good agreement with the Jarrett et al. (2013) calibrations is encouraging, as their sample consists of 17 well-resolved, nearby galaxies for which measurement uncertainties are minimal. (In fact, the small difference is consistent with the random variation expected in the average for small sample of 17 objects.) Our calibration generalizes their result by extending the dynamic range in stellar mass and star-formation rate by an order of magnitude upward and using a sample of several hundred thousand galaxies.

Our 12μm and 22μm SFR conversions are lower by, respectively, 0.22 dex and 0.10 dex compared to Lee et al. (2013), who use the Brinchmann et al. (2004) SFRs.[8] Part of this offset can be attributed to the systematic differences between our SFR estimates and those of Brinchmann et al. (2004) (see Sec 4.1). Additional factors are the differences in sample selection and modeling technique. We select star-forming galaxies on the basis of their optical colors, whereas Lee et al. (2013) select galaxies with large 22μm luminosities. Moreover, not all mid-IR radiation traces SF, which is taken into account in our modeling, whereas Lee et al. (2013) simply use total mid-IR luminosity as a SF tracer.

[8] These differences include the appropriate correction from Salpeter to Chabrier IMF for the Lee et al. (2013) conversions.

4.3. *A Fresh View on Bimodality*

Assessing bi-modality in the galaxy population requires a sample that is corrected for completeness and sufficient sensitivity in the star-formation tracer to separate star-forming and passive galaxies. We compare the magnitude in r band with the WISE bands at different redshift and find that the mass completeness limit of our sample is set by the SDSS r-band spectroscopic limit for all redshifts: the fraction of galaxies above the mass limit without WISE counterparts is less than 1%. The completeness limit at a given redshift is found by identifying the most massive galaxies with magnitudes near the limit. As such we find that the mass completeness limit depends on redshift as $\log M_{limit} = 10.6 + 2.28 \log(z/0.1)$. The mass limit is such that actively SF-ing galaxies always have significant 12μm detections; that is, if a galaxy is not detected at 12 μm it must be a quiescent galaxy. In other words, the upper limit on SFR is useful is the sense that it allows us to distinguish between SF-ing and quiescent galaxies. Using the mass limit, a galaxy of a given mass is assigned a V_{max} value assuming a survey area of 8,032 square degrees. These values are given in Table 2.

In Figure 11 we show the SFR-M_* distribution of the 363,774 galaxies above our mass limit and with FLAG = 1 (see Section 3.4). The sequence of star-forming galaxies (a.k.a. the Main Sequence) – indicated in orange – is quantified by the median in 0.2-wide stellar mass bins. We fit these median values with a power law and find:

$$\log SFR/(M_\odot yr^{-1}) = 0.80 \log M_*/(10^{10}\ M_\odot) - 0.23. \qquad (4)$$

We define the scatter in the Main Sequence as the 84%-50%-ile range, which is 0.39 dex. The downward scatter (50%-16%-ile range) is larger (0.64 dex), but this number is difficult to interpret due to the imperfect separation of star-forming and quiescent galaxies. This uncertainty is not (only) due to limited fidelity in our color-color classification, but also due to the natural variation in SF activity.

For comparison, when we apply our fitting technique using the Brinchmann et al. (2004) values for stellar masses and SFRs, we find:

$$\log SFR/(M_\odot yr^{-1}) = 0.75 \log M_*/(10^{10}\ M_\odot) - 0.03. \qquad (5)$$

Our fit is slightly steeper, but more importantly, has a 0.2 dex higher intercept at $M_* = 10^{10}\ M_\odot$ and a larger scatter (0.39 dex vs. 0.31 dex). The larger scatter can perhaps be attributed to the more direct measurement of highly obscured star formation when using mid-IR luminosities as a tracer as opposed to the optical emission lines. We note that the random uncertainties in our SFR estimates (typically, 0.18 dex) are much smaller than the scatter, indicating a large intrinsic scatter around the "main sequence" relation. This is in stark contrast with the measurements from Brinchmann et al. (2004): their typical uncertainty is 0.30 dex – the same as the scatter

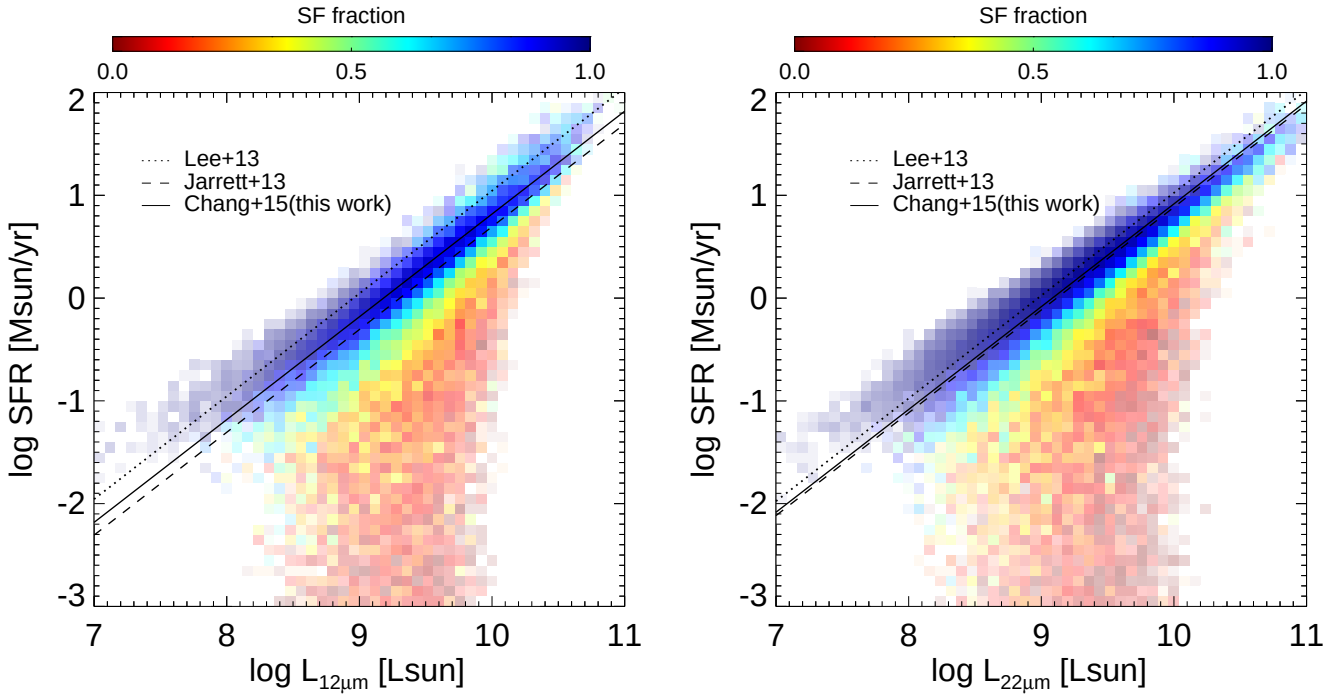

FIG. 10.— SFR vs. rest-frame 12μm and 22μm luminosities for galaxies that have significant detections in both WISE bands. The data are binned and color-coded according to the fraction of star-forming galaxies as defined in the color-color diagram shown in Figure 2. For star-forming galaxies we produce a linear fit, as i ndicated by the solid lines. For comparison we show equivalent fits from Lee et al. (2013) and Jarrett et al. (2013). The SFRs are matched to Chabrier (2003) IMF.

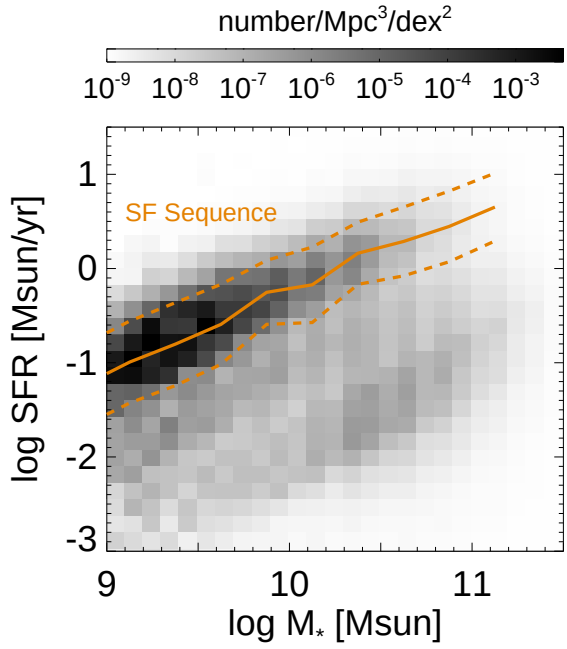

FIG. 11.— Distribution of galaxies above our (redshift-dependent) mass completness limit in the SFR vs M_* plane. The mass limit described in Section 4.3 is such that all galaxies on or near the the SF-ing sequence have significant detections at 12μm. The star-forming sequence is shown in orange, where the dashed lines show the 1σ scatter, as explained in Section 4.3. In order to visualize the SFR bimodality we adopt the 1-σ upper limits on the SFR for galaxies where the SFR estimate is more uncertain than 0.39 dex. Consequently, quiescent galaxies in this plot are placed at the upper limit of the true SFR. The gray scale represents the number of galaxies after weighing by $1/V_{max}$.

– implying zero intrinsic scatter. We conclude that the the star-forming sequence as revealed by the WISE photometry is less tight than what is inferred from optical SDSS spectra.

The bi-modality seen in Figure 11 in our inferred SFR-M_* distribution can be directly compared with Figure 17 and 24 from Brinchmann et al. (2004), where the SFRs are inferred from nebular emission lines strengths, and with Figure 15 from Salim et al. (2007), where the SFRs are inferred from UV luminosities. The color coding used in Figure 2 is based on the separation of star forming and non-star forming galaxies in Figure 11: non-star forming galaxies are those that lie below the sequence by 2 times the scatter or more. This confirms that the two-color diagram is a simple yet very effective tool to separate dusty from passive galaxies.

Finally, it is of interest to explore the distribution of SF in relation to traditional tools to probe SF activity across the galaxy population, such as the color-mass diagram, the BPT diagram (Baldwin et al. 1981), and the Hδ-D4000 relation (Kauffmann et al. 2003). In Figure 12 we show the $g-r$ vs. stellar mass distribution in three different ways: weighed by number density, weighed by SFR density, and weighed by stellar mass density. The first panel shows the well-known bimodality in the form of a red sequence and a blue cloud. We have also indicated the intermediate region often called the green valley, which has been argued to contain galaxies that are transitioning from blue to red (e.g., Schawinski et al. 2007). However, as most recently shown by Taylor et al. (2015), many galaxies in this region are reddened because of dust (also see, e.g., Conselice 2006) and not primarily due to a reduced level of SF. This is illustrated in the second panel, which shows that the galaxies in the green valley region – and not the more numerous,

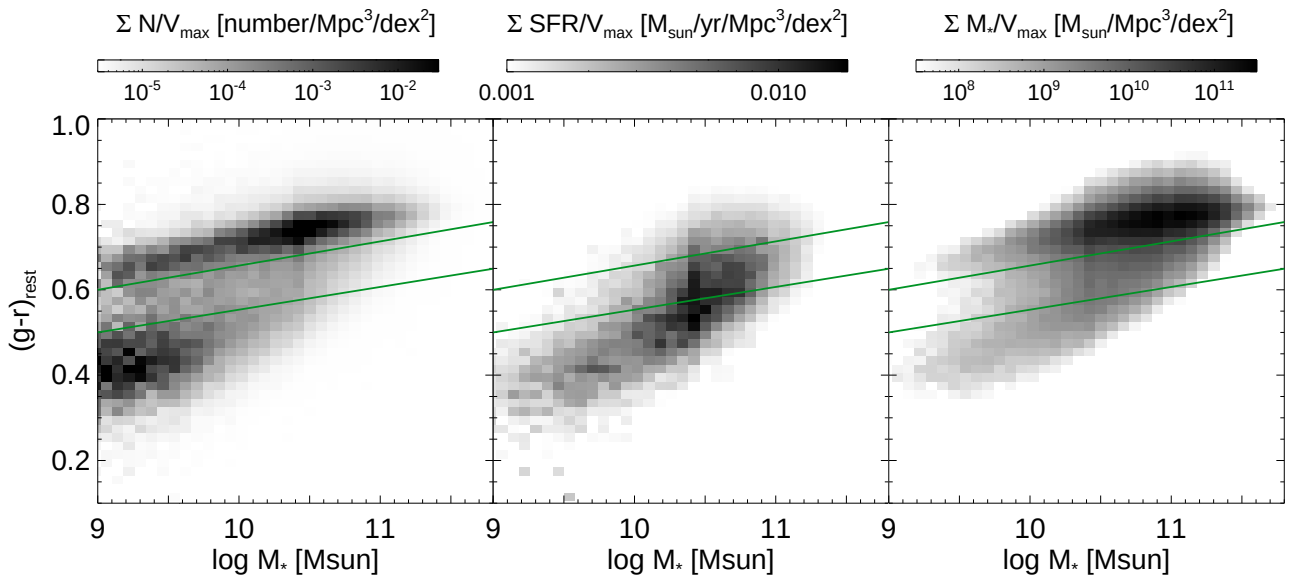

FIG. 12.— Left: comoving number density distribution of galaxies in the stellar mass vs. rest-frame $g-r$ plane. The grey scale reflects the numbers of galaxies in each bin after weighing with $1/V_{max}$. Middle: the grey scale reflects the SFR density. Right: the grey scale reflects the stellar mass density. Apparently, the green valley provides the most fertile ground for star formation as indicated by the green line.

fainter blue galaxies – dominate the total SF budget of the present-day universe. On the other hand, these massive, SF-ing galaxies do not dominate the stellar mass budget, as is shown in the third panel. The absence of a dominant population of massive, SF-ing galaxies and a general dearth of massive, disk-like galaxies (van der Wel et al. 2009) implies that their SFRs cannot be sustained for long (Schawinski et al. 2014).

In Figure 13 we show the SFR distribution in the BPT and $H\delta$-$D_n(4000)$ diagrams in three different mass bins. In the left-hand panels, we show the BPT diagram at different stellar mass bins. For the low stellar mass sample, most population are star-forming galaxies and most SF activities are also occur in SF region. For higher stellar mass bins, the population moves to composite galaxies and even low-ionization nuclear emission-line region (LINER), but the SF activities still occur between star-forming and composite regions.

In the right-hand panels we see, like Kauffmann et al. (2003), that the strength of the 4000Åbreak, tracing evolved stellar populations (>1 Gyr), is anti-correlated with $H\delta$, tracing the presence of younger stellar populations (age <1 Gyr). Not surprisingly, SF mostly occurs in galaxies with generally young populations. For low-mass galaxies the SF-ing population is representative of the general population, but for high-mass galaxies the SF-ing galaxies represent a tail of outliers, as most galaxies are old and quiescent. Still, high-mass SF-ing galaxies are older than their low-mass counterparts. This can be interpreted as evidence for an increasingly prominent bulge, while SF activity in the disk is similar to that in the disks of lower-mass galaxies as argued by Abramson et al. (2014). However, it could also signal a decline in SF activity as suggested by Schawinski et al. (2014).

A detailed exploration of the processes that drive SF evolution is beyond the scope of this paper, but we hope that the community will take advantage of the mid-IR based SFR estimates published here to distinguish further between reddening by dust, age, and reduced SF activity.

5. SUMMARY

We revisit the measurement of stellar masses and star-formation rates for the SDSS spectroscopic galaxy sample after adding 4-band photometry from WISE for the wavelength range $3-22\mu$m. We benefit from this wavelength extension by adopting the latest, state-of-the-art SED modeling approach (MAGPHYS da Cunha et al. 2008), which includes the self-consistent treatment of dust attenuation and emission and a wide range of star formation histories. The resulting SFR esimates are mostly based on PAH emission and thermal dust radiation, and, therefore, are complementary to the nebular emission line-derived estimates from (Brinchmann et al. 2004). In Section 4.2 we provide new calibrations for the conversion of monochromatic 12μm and 22μm luminosities into SFRs.

The new M_* and SFR estimates show the well-established bi-modality in SF activity. A first application is the verification of the cruder color-color separation of SF-ing and quiescent galaxies that is often used at higher redshifts. We confirm that the $U-V$-$V-J$ (or, alternatively, $u-r$-$r-z$, as in Figure 11) color-color separation has a 89% success rate in identifying SF-ing and quiescent galaxies.

We also fit the relation between SFR and M_* (the SF-ing sequence, or SF-ing Main Sequence). Our sequence is slightly steeper than previous studies based on SDSS galaxies, and has a higher normalization and scatter. We attribute these differences to our new SFR estimates that now include dust emission and also to some extent the uncertainty in establishing a purely star-forming sample (i.e. without contamination from quiescent galaxies). L_* falaxies contribute most to the cosmic SF density, and these typically have optical colors that are in between those of the traditional red squence and blue cloud (Figure 12) as a result of dust attenuation, not because of reduced star-formation activity.

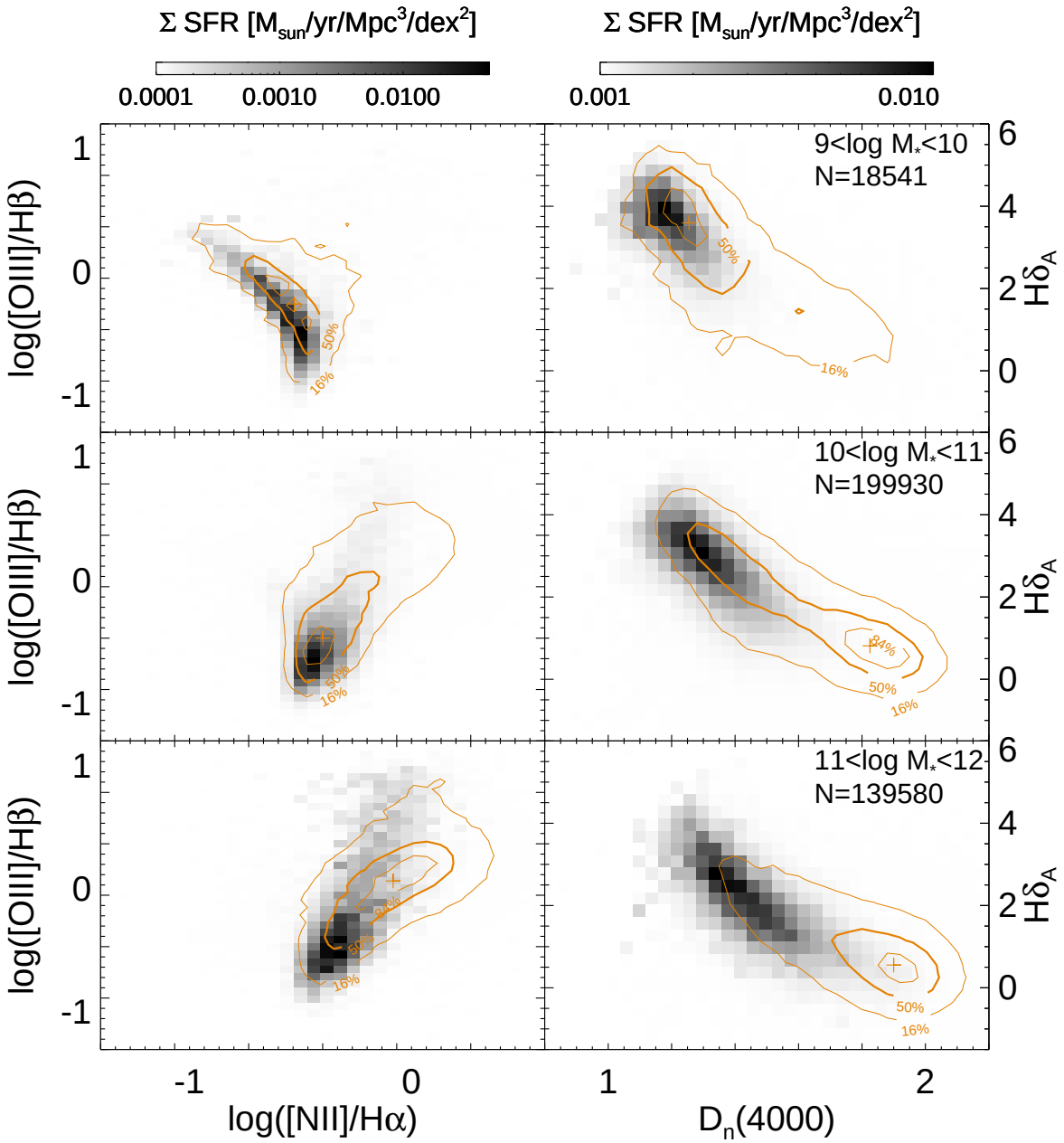

FIG. 13.— Number density (contours) and SFR density distribution (grey scale) in the BPT diagram (left, only galaxies with detected emission lines) and $H\delta$-$D_n(4000)$ (right). From top to bottom we show 3 different mass bins.

As a service to the community we make our SDSS+WISE matched photometry catalog as well as the SED fitting results publicly available.

We thank the anonymous referee for useful comments to improve this paper. Y.-Y. Chang was funded by the IMPRS for Astronomy & Cosmic Physics at the University of Heidelberg and the Marie Curie Initial Training Network ELIXIR of the European Commission under contract PITN-GA-2008-214227. E. da Cunha acknowledges funding through the ERC grant 'Cosmic Dawn'.

Funding for the SDSS and SDSS-II has been provided by the Alfred P. Sloan Foundation, the Participating Institutions, the National Science Foundation, the U.S. Department of Energy, the National Aeronautics and Space Administration, the Japanese Monbukagakusho, the Max Planck Society, and the Higher Education Funding Council for England. The SDSS Web Site is http://www.sdss.org/. The SDSS is managed by the Astrophysical Research Consortium for the Participating Institutions. The Participating Institutions are the American Museum of Natural History, Astrophysical Institute Potsdam, University of Basel, University of Cambridge, Case Western Reserve University, University

of Chicago, Drexel University, Fermilab, the Institute for Advanced Study, the Japan Participation Group, Johns Hopkins University, the Joint Institute for Nuclear Astrophysics, the Kavli Institute for Particle Astrophysics and Cosmology, the Korean Scientist Group, the Chinese Academy of Sciences (LAMOST), Los Alamos National Laboratory, the Max-Planck-Institute for Astronomy (MPIA), the Max-Planck-Institute for Astrophysics (MPA), New Mexico State University, Ohio State University, University of Pittsburgh, University of Portsmouth, Princeton University, the United States Naval Observatory, and the University of Washington.

This publication makes use of data products from the Wide-field Infrared Survey Explorer, which is a joint project of the University of California, Los Angeles, and the Jet Propulsion Laboratory/California Institute of Technology, funded by the National Aeronautics and Space Administration

The Herschel-ATLAS is a project with Herschel, which is an ESA space observatory with science instruments provided by European-led Principal Investigator consortia and with important participation from NASA. The H-ATLAS website is http://www.h-atlas.org/.

REFERENCES

Abramson, L. E., Kelson, D. D., Dressler, A., Poggianti, B., Gladders, M. D., Oemler, Jr., A., & Vulcani, B. 2014, ApJ, 785, L36 [4.3]
Adelman-McCarthy, J. K., et al. 2008, ApJS, 175, 297 [1, 2]
Aniano, G., Draine, B. T., Gordon, K. D., & Sandstrom, K. 2011, PASP, 123, 1218 [2]
Baldry, I. K., et al. 2012, MNRAS, 421, 621 [1]
Baldwin, J. A., Phillips, M. M., & Terlevich, R. 1981, PASP, 93, 5 [4.3]
Blanton, M. R., et al. 2005, AJ, 129, 2562 [1, 2]
Bressan, A., et al. 2006, ApJ, 639, L55 [4.2]
Brinchmann, J., Charlot, S., White, S. D. M., Tremonti, C., Kauffmann, G., Heckman, T., & Brinkmann, J. 2004, MNRAS, 351, 1151 [1, 4.1, 4.2, 4.2, 4.3, 4.3, 5]
Brown, M. J. I., et al. 2014, ApJS, 212, 18 [1]
Bruzual, G., & Charlot, S. 2003, MNRAS, 344, 1000 [3.1]
Chabrier, G. 2003, PASP, 115, 763 [1, 10]
Charlot, S., & Fall, S. M. 2000, ApJ, 539, 718 [4.1]
Charlot, S., & Longhetti, M. 2001, MNRAS, 323, 887 [1]
Chary, R., & Elbaz, D. 2001, ApJ, 556, 562 [3.1]
Cluver, M. E., et al. 2014, ApJ, 782, 90 [1]
Conselice, C. J. 2006, MNRAS, 373, 1389 [4.3]
da Cunha, E., Charlot, S., Dunne, L., Smith, D., & Rowlands, K. 2012, in IAU Symposium, Vol. 284, IAU Symposium, ed. R. J. Tuffs & C. C. Popescu, 292–296 [3.1]
da Cunha, E., Charlot, S., & Elbaz, D. 2008, MNRAS, 388, 1595 [1, 3.1, 5, 2]
Donoso, E., et al. 2012, ApJ, 748, 80 [1, 2]
Eales, S., et al. 2010, PASP, 122, 499 [3.3]
Holden, B. P., van der Wel, A., Rix, H.-W., & Franx, M. 2012, ApJ, 749, 96 [3.1]
Ibar, E., et al. 2010, MNRAS, 409, 38 [3.3]
Jarrett, T. H., et al. 2013, AJ, 145, 6 [1, 4.2, 10]
Kauffmann, G., et al. 2003, MNRAS, 341, 33 [4.3]
[1]
Lee, J. C., Hwang, H. S., & Ko, J. 2013, ApJ, 774, 62 [1, 4.2, 4.2, 8, 10]
Li, H.-N., Wu, H., Cao, C., & Zhu, Y.-N. 2007, AJ, 134, 1315 [1]
Meidt, S. E., et al. 2014, ApJ, 788, 144 [1]
Padmanabhan, N., et al. 2008, ApJ, 674, 1217 [1, 2]
Pascale, E., et al. 2011, MNRAS, 415, 911 [3.3]
Peng, C. Y., Ho, L. C., Impey, C. D., & Rix, H.-W. 2010, AJ, 139, 2097 [2]
Rieke, G. H., Alonso-Herrero, A., Weiner, B. J., Pérez-González, P. G., Blaylock, M., Donley, J. L., & Marcillac, D. 2009, ApJ, 692, 556 [4.2]
Rigby, E. E., et al. 2011, MNRAS, 415, 2336 [3.3]
Salim, S., et al. 2007, ApJS, 173, 267 [1, 4.3]
Schawinski, K., et al. 2007, ApJS, 173, 512 [4.3]
—. 2014, MNRAS, 440, 889 [4.3]
Schlafly, E. F., & Finkbeiner, D. P. 2011, ApJ, 737, 103 [2, 4.1]
Simard, L., Mendel, J. T., Patton, D. R., Ellison, S. L., & McConnachie, A. W. 2011, ApJS, 196, 11 [2, 3.4]
Smith, D. J. B., et al. 2011, MNRAS, 416, 857 [3.3]
—. 2012, MNRAS, 427, 703 [3.2]
Taylor, E. N., et al. 2011, MNRAS, 418, 1587 [1]
—. 2015, MNRAS, 446, 2144 [4.3]
van der Wel, A., Rix, H.-W., Holden, B. P., Bell, E. F., & Robaina, A. R. 2009, ApJ, 706, L120 [4.3]
Vulcani, B., et al. 2014, MNRAS, 441, 1340 [2]
Wen, X.-Q., Wu, H., Zhu, Y.-N., Lam, M. I., Wu, C.-J., Wicker, J., Long, R. J., & Zhao, Y.-H. 2014, MNRAS, 438, 97 [1]
Wen, X.-Q., Wu, H., Zhu, Y.-N., Lam, M. I., Wu, C.-J., Wicker, J., & Zhao, Y.-H. 2013, MNRAS, 433, 2946 [1]
Wright, E. L., et al. 2010, AJ, 140, 1868 [1]
Yan, L., et al. 2013, AJ, 145, 55 [2]
Zhu, Y.-N., Wu, H., Li, H.-N., & Cao, C. 2010, Research in Astronomy and Astrophysics, 10, 329

TABLE 1
Input Catalog

Column Name	Format	Unit	Column Description
ID	LONG	-	NYU-VAGC catalog index
RA	DOUBLE	deg	J2000 R.A. [deg] from NYU-VAGC (r-band)
DEC	DOUBLE	deg	J2000 Dec. [deg] from NYU-VAGC (r-band)
REDSHIFT	DOUBLE	-	Redshift from the NYU-VAGC spectroscopic catalog
PLATE	LONG	-	SDSS plate from NYU-VAGC
MJD	LONG	-	SDSS mjd from NYU-VAGC
FIBERID	LONG	-	SDSS fiberid from NYU-VAGC
DESIGNATION	STRING	-	ALLWISE designation
FLUX0_U	DOUBLE	Jy	u-band Flux before corrections
FLUX0_U_E	DOUBLE	Jy	Uncertainty of u-band flux before corrections
FLUX0_G	DOUBLE	Jy	g-band flux before corrections
FLUX0_G_E	DOUBLE	Jy	Uncertainty of g-band flux before corrections
FLUX0_R	DOUBLE	Jy	r-band flux before corrections
FLUX0_R_E	DOUBLE	Jy	Uncertainty of r-band flux before corrections
FLUX0_I	DOUBLE	Jy	i-band flux before corrections
FLUX0_I_E	DOUBLE	Jy	Uncertainty of i-band flux before corrections
FLUX0_Z	DOUBLE	Jy	z-band flux before corrections
FLUX0_Z_E	DOUBLE	Jy	Uncertainty of z-band flux before corrections
FLUX0_W1	DOUBLE	Jy	$W1$-band flux before corrections
FLUX0_W1_E	DOUBLE	Jy	Uncertainty $W1$-band of flux before corrections
FLUX0_W2	DOUBLE	Jy	$W2$-band flux before corrections
FLUX0_W2_E	DOUBLE	Jy	Uncertainty $W2$-band of flux before corrections
FLUX0_W3	DOUBLE	Jy	$W3$-band flux before corrections
FLUX0_W3_E	DOUBLE	Jy	Uncertainty $W3$-band of flux before corrections
FLUX0_W4	DOUBLE	Jy	$W4$-band flux before corrections
FLUX0_W4_E	DOUBLE	Jy	Uncertainty $W4$-band of flux before corrections
FLUX_U	DOUBLE	Jy	u-band Flux after corrections
FLUX_U_E	DOUBLE	Jy	Uncertainty of u-band flux after corrections
FLUX_G	DOUBLE	Jy	g-band Flux after corrections
FLUX_G_E	DOUBLE	Jy	Uncertainty of g-band flux after corrections
FLUX_R	DOUBLE	Jy	r-band Flux after corrections
FLUX_R_E	DOUBLE	Jy	Uncertainty of r-band flux after corrections
FLUX_I	DOUBLE	Jy	i-band Flux after corrections
FLUX_I_E	DOUBLE	Jy	Uncertainty of i-band flux after corrections
FLUX_Z	DOUBLE	Jy	z-band Flux after corrections
FLUX_Z_E	DOUBLE	Jy	Uncertainty of z-band flux after corrections
FLUX_W1	DOUBLE	Jy	$W1$-band Flux after corrections
FLUX_W1_E	DOUBLE	Jy	Uncertainty $W1$-band of flux after corrections
FLUX_W2	DOUBLE	Jy	$W2$-band Flux after corrections
FLUX_W2_E	DOUBLE	Jy	Uncertainty $W2$-band of flux after corrections
FLUX_W3	DOUBLE	Jy	$W3$-band Flux after corrections
FLUX_W3_E	DOUBLE	Jy	Uncertainty $W3$-band of flux after corrections
FLUX_W4	DOUBLE	Jy	$W4$-band Flux after corrections
FLUX_W4_E	DOUBLE	Jy	Uncertainty $W4$-band of flux after corrections
EXTIN_U	DOUBLE	*mag*	Galactic extinction correction for u-band
EXTIN_G	DOUBLE	*mag*	Galactic extinction correction for g-band
EXTIN_R	DOUBLE	*mag*	Galactic extinction correction for r-band
EXTIN_I	DOUBLE	*mag*	Galactic extinction correction for i-band
EXTIN_Z	DOUBLE	*mag*	Galactic extinction correction for z-band

TABLE 2
Output Catalog

Column Name	Format	Unit	Column Description
LMASS_2_5	FLOAT	$\log M_\odot$	log stellar mass (2.5th percentile)
LMASS_16	FLOAT	$\log M_\odot$	log stellar mass (16th percentile)
LMASS_50	FLOAT	$\log M_\odot$	log stellar mass (50th percentile)
LMASS_84	FLOAT	$\log M_\odot$	log stellar mass (84th percentile)
LMASS_97_5	FLOAT	$\log M_\odot$	log stellar mass (97.5th percentile)
LSFR_2_5	FLOAT	$\log M_\odot/yr$	log SFR (2.5th percentile)
LSFR_16	FLOAT	$\log M_\odot/yr$	log SFR (16th percentile)
LSFR_50	FLOAT	$\log M_\odot/yr$	log SFR (50th percentile)
LSFR_84	FLOAT	$\log M_\odot/yr$	log SFR (84th percentile)
LSFR_97_5	FLOAT	$\log M_\odot/yr$	log SFR (97.5th percentile)
LSSFR_2_5	FLOAT	$\log 1/yr$	log specific SFR (2.5th percentile)
LSSFR_16	FLOAT	$\log 1/yr$	log specific SFR (16th percentile)
LSSFR_50	FLOAT	$\log 1/yr$	log specific SFR (50th percentile)
LSSFR_84	FLOAT	$\log 1/yr$	log specific SFR (84th percentile)
LSSFR_97_5	FLOAT	$\log 1/yr$	log specific SFR (97.5th percentile)
LDUST_2_5	FLOAT	$\log L_\odot$	log dust luminosity (2.5th percentile)
LDUST_16	FLOAT	$\log L_\odot$	log dust luminosity (16th percentile)
LDUST_50	FLOAT	$\log L_\odot$	log dust luminosity (50th percentile)
LDUST_84	FLOAT	$\log L_\odot$	log dust luminosity (84th percentile)
LDUST_97_5	FLOAT	$\log L_\odot$	log dust luminosity (97.5th percentile
MU_2_5	FLOAT	-	dust attenuation parameter in da Cunha et al. (2008) (2.5th percentile)
MU_16	FLOAT	-	dust attenuation parameter in da Cunha et al. (2008) (16th percentile)
MU_50	FLOAT	-	dust attenuation parameter in da Cunha et al. (2008) (50th percentile)
MU_84	FLOAT	-	dust attenuation parameter in da Cunha et al. (2008) (84th percentile)
MU_97_5	FLOAT	-	dust attenuation parameter in da Cunha et al. (2008) (97.5th percentile)
TAUV_2_5	FLOAT	-	dust attenuation parameter in da Cunha et al. (2008) (2.5th percentile)
TAUV_16	FLOAT	-	dust attenuation parameter in da Cunha et al. (2008) (16th percentile)
TAUV_50	FLOAT	-	dust attenuation parameter in da Cunha et al. (2008) (50th percentile)
TAUV_84	FLOAT	-	dust attenuation parameter in da Cunha et al. (2008) (84th percentile)
TAUV_97_5	FLOAT	-	dust attenuation parameter in da Cunha et al. (2008) (97.5th percentile)
V_MAX	DOUBLE	Mpc^3	Maximum volume for LMASS_50
LREST_U	DOUBLE	$\log L_\odot$	Rest-frame u-band Luminosity
LREST_G	DOUBLE	$\log L_\odot$	Rest-frame g-band Luminosity
LREST_R	DOUBLE	$\log L_\odot$	Rest-frame r-band Luminosity
LREST_I	DOUBLE	$\log L_\odot$	Rest-frame i-band Luminosity
LREST_Z	DOUBLE	$\log L_\odot$	Rest-frame z-band Luminosity
LREST_W1	DOUBLE	$\log L_\odot$	Rest-frame $W1$-band Luminosity
LREST_W2	DOUBLE	$\log L_\odot$	Rest-frame $W2$-band Luminosity
LREST_W3	DOUBLE	$\log L_\odot$	Rest-frame $W3$-band Luminosity
LREST_W4	DOUBLE	$\log L_\odot$	Rest-frame $W4$-band Luminosity
FLAG_R	INT	-	1: Simard radius; 2: deVaucouleurs radius; 3: exponential radius; 0: no radius
FLAG_W	INT	-	1: single optical matched in WISE; 2: >1 counterparts within 6"; 0: not matched
FLAG_W1	INT	-	1: detected W1 (SNR>2); 2: upper limit on W1; 0: no W1 data
FLAG_W2	INT	-	1: detected W2 (SNR>2); 2: upper limit on W2; 0: no W2 data
FLAG_W3	INT	-	1: detected W3 (SNR>2); 2: upper limit on W3; 0: no W3 data
FLAG_W4	INT	-	1: detected W4 (SNR>2); 2: upper limit on W4; 0: no W4 data
FLAG_CHI2	INT	-	1: $\chi^2 < 3$ for best-fit model; 0: $\chi^2 > 3$ for best-fit model
FLAG	INT	-	1: good fit (FLAG_R=1; FLAG_W?=1 or 2; FLAG_CHI2=1; $z < 0.2$); 0: others